Astronomy
&
Astrophysics

HDO and SO$_2$ thermal mapping on Venus

V. Evidence for a long-term anti-correlation

T. Encrenaz[1], T. K. Greathouse[2], E. Marcq[3], H. Sagawa[4], T. Widemann[1], B. Bézard[1], T. Fouchet[1], F. Lefèvre[3],
S. Lebonnois[5], S. K. Atreya[6], Y. J. Lee[7], R. Giles[8], S. Watanabe[9], W. Shao[10], X. Zhang[10], and C. J. Bierson[10]

[1] LESIA, Observatoire de Paris, PSL University, CNRS, Sorbonne Université, Université de Paris, 92195 Meudon, France
   e-mail: therese.encrenaz@obspm.fr
[2] SwRI, Div. 15, San Antonio, TX 78228, USA
[3] LATMOS/IPSL, UVSQ Université Paris-Saclay, Sorbonne Université, CNRS, 78280 Guyancourt, France
[4] Kyoto Sangyo University, Kyoto 603-8555, Japan
[5] LMD/IPSL, Sorbonne University, ENS, PSL University, Ecole Polytechnique, University Paris Saclay, CNRS, 75252 Paris Cedex 05, France
[6] Planetary Science Laboratory, University of Michigan, Ann Arbor MI 48109-2143, USA
[7] Zentrum fuer Astronomie und Astrophysik, Technische Universitaet Berlin, Hardenbergstr. 36, 10623 Berlin, Germany
[8] Jet Propulsion Laboratory, Pasadena, CA 91109, USA
[9] Hokkaido Information University, Hokkaido 069-8585, Japan
[10] Department of Earth and Planetary Sciences, University of California, Santa Cruz, CA 95064, USA

ABSTRACT

Since January 2012, we have been monitoring the behavior of sulfur dioxide and water on Venus, using the Texas Echelon Cross-Echelle Spectrograph imaging spectrometer at the NASA InfraRed Telescope Facility (IRTF, Mauna Kea Observatory). Here, we present new data recorded in February and April 2019 in the 1345 cm^{-1} (7.4 μm) spectral range, where SO$_2$, CO$_2$, and HDO (used as a proxy for H$_2$O) transitions were observed. The cloud top of Venus was probed at an altitude of about 64 km. As in our previous studies, the volume mixing ratio (vmr) of SO$_2$ was estimated using the SO$_2$/CO$_2$ line depth ratio of weak transitions; the H$_2$O volume mixing ratio was derived from the HDO/CO$_2$ line depth ratio, assuming a D/H ratio of 200 times the Vienna standard mean ocean water. As reported in our previous analyses, the SO$_2$ mixing ratio shows strong variations with time and also over the disk, showing evidence for the formation of SO$_2$ plumes with a lifetime of a few hours; in contrast, the H$_2$O abundance is remarkably uniform over the disk and shows moderate variations as a function of time. We have used the 2019 data in addition to our previous dataset to study the long-term variations of SO$_2$ and H$_2$O. The data reveal a long-term anti-correlation with a correlation coefficient of -0.80; this coefficient becomes -0.90 if the analysis is restricted to the 2014–2019 time period. The statistical analysis of the SO$_2$ plumes as a function of local time confirms our previous result with a minimum around 10:00 and two maxima near the terminators. The dependence of the SO$_2$ vmr with respect to local time shows a higher abundance at the evening terminator with respect to the morning. The dependence of the SO$_2$ vmr with respect to longitude exhibits a broad maximum at 120–200° east longitudes, near the region of Aphrodite Terra. However, this trend has not been observed by other measurements and has yet to be confirmed.

Key words. planets and satellites: atmospheres – planets and satellites: terrestrial planets – infrared: planetary systems

1. Introduction

The atmospheric chemistry of Venus is driven by the cycles of water and sulfur dioxide (Krasnopolsky 1986, 2007, 2010; Mills et al. 2007; Zhang et al. 2012). Below the clouds, both species are present with relatively large abundances (about 30 ppmv and 130 ppmv respectively, Bézard & De Bergh 2012, Marcq et al. 2018) and, at low latitude, they are transported upward by Hadley convection. Following the SO$_2$ photodissociation and the combination of SO$_3$ with H$_2$O, sulfuric acid H$_2$SO$_4$ is formed and condenses as the main component of the cloud deck. Above the cloud top, the volume mixing ratios of H$_2$O and SO$_2$ drop drastically to about 1–3 ppmv (Fedorova et al. 2008; Belyaev et al. 2012) and 10–1000 ppbv (Zasova et al. 1993; Marcq et al. 2013, 2020; Vandaele et al. 2017a,b), respectively.

The water and sulfur dioxide cycles have been extensively monitored over several decades, using Pioneer Venus, the Venera

15 spacecraft, Venus Express, and Akatsuki by imaging and spectroscopy in the ultraviolet and infrared ranges. As a complement to these datasets, we have been using imaging spectroscopy in the thermal infrared since 2012 to map SO$_2$ and H$_2$O at the cloud top of Venus and to monitor the behavior of these two species as a function of time, both in the short term (a few hours) and the long term (years). Thirteen runs were recorded between 2012 and 2019. The results of the first 11 runs (January 2012– September 2018) have been presented in Encrenaz et al. (2012, 2013, 2016, 2019), which are referred as E12, E13, E16, and E19, hereafter. The main result of these studies is that SO$_2$ and H$_2$O exhibit very different behaviors. We note that H$_2$O is always uniformly distributed over the disk and shows moderate variations in the long term. In contrast, the SO$_2$ maps most often show sporadic plumes which appear and disappear within a time scale of a few hours. The disk-integrated SO$_2$ abundance shows strong variations over the long term, with a contrast factor of about 10

between the minimum value observed in February 2014 and the maximum value from July 2018.

In this paper, we first describe the observations performed in February and April 2019 (Sect. 2). Then we use the whole TEXES data set (2012–2019) at 7.4 μm to study the long-term evolution of H_2O and SO_2 (Sect. 3). Finally we update our statistical analysis of the SO_2 plumes (E19), regarding their appearance as a function of latitude, longitude and local time (Sect. 4). The results are discussed in Sect. 5 and the conclusions are summarized in Sect. 6.

2. Observations

2.1. The data

TEXES (Texas Echelon Cross Echelle Spectrograph) is an imaging high-resolution thermal infrared spectrometer in operation at the NASA InfraRed telescope Facility (Lacy et al. 2002), which combines high spectral capabilities ($R = 80\,000$ at 7 μm) and spatial capabilities (around 1 arcsec). As for our previous observations, we selected the 1342–1348 cm^{-1} (7.4 μm) interval in order to optimize the number of weak and strong transitions of SO_2, HDO and CO_2. The diameter of Venus was 17 arcsec in February 2019 and 12 arcsec in April 2019. The Doppler shift, at 1345 cm^{-1}, was between -0.045 and -0.043 cm^{-1} in February 2019 and between $+0.045$ and $+0.043$ cm^{-1} in April 2019. The length and the width of the slit were 6.0 and 1.0 arcsec respectively at 7.4 μm.

As we did previously, we aligned the slit along the north-south celestial axis and we shifted it from west to east, with a step of half the slit width and an integration time of 2 s per position to cover the planet in longitude from limb to limb, and to add a few pixels on the sky beyond each limb for sky subtraction. Since the rotation axis of Venus is close to the celestial axis, each scan corresponds to a given latitude range of about 6 arcsec. As the diameter of Venus was always larger than the slit length, we multiplied the scans to cover the full latitude range from north to south with some overlap. Table 1 summarizes the TEXES observations in February and April 2019. This table lists the maps which were obtained at 1345 cm^{-1}, with, in each case, the time of beginning and end of the observation, its mid-time, and the number of scans used to build the maps. A scan at a given latitude was usually repeated at least twice. Typically, twelve scans were used to cover the whole latitude range; their number varied according to the meteorological conditions; in some cases, some scans were removed if the terrestrial atmospheric transmission is too strong.

The TEXES data cubes were calibrated using the standard radiometric method (Lacy et al. 2002, Rohlfs & Wilson 2004). Calibration frames consisting of three measurements (black chopper blade, sky and low-emissiviy chopper blade) were systematically taken before each observing scan, and the difference (black-sky) was taken as a flat field. If the temperature of the black blade, the telescope and the sky are equal, this method corrects both telescope and atmospheric emissions. The atmospheric correction, however, is not complete for all terrestrial atmospheric lines, partly because these lines are not all formed at the same atmospheric levels, and thus have different temperatures. For these reasons, we did not try to correct the terrestrial atmospheric features and we selected SO_2 and CO_2 lines located outside these features. In the case of HDO, it was not always possible; this is why, in some cases, HDO maps could not be retrieved (see below).

Figure 1 shows the geometrical configurations of the disk of Venus during the two runs of February and April 2019, which

Table 1. Summary of TEXES observations of February and April 2019.

Date of obs.	Map	Start time (UT)	End time (UT)	Mid time (UT)	Number of scans
2019/02/12	a	20:10	20:34	20:22	12
2019/02/12	b	21:24	20:52	21:38	14
2019/02/13	a	20:01	20:30	20:16	13
2019/02/13	b	21:14	21:41	20:28	14
2019/02/14	a	20:00	20:25	20:13	12
2019/02/14	b	21:10	21:34	20:22	12
2019/02/16	a	16:32	16:56	16:44	12
2019/02/16	b	17:50	18:15	18:03	12
2019/02/16	c	19:03	19:30	19:17	14
2019/02/16	d	20:18	20:41	20:30	12
2019/02/16	e	21:30	21:54	21:42	12
2019/02/16	f	22:47	22:54	22:51	4
2019/02/17	a	20:02	20:27	20:15	11
2019/02/17	b	21:14	21:38	21:26	12
2019/02/17	c	22:26	22:50	22:38	12
2019/02/18	a	20:09	20:34	20:22	11
2019/02/18	b	21:42	22:06	21:54	11
2019/04/15	a	17:29	17:47	17:38	10
2019/04/15	b	18:32	18:46	18:39	8
2019/04/15	c	19:24	19:38	19:31	8
2019/04/15	d	20:42	21:03	20:53	7
2019/04/16	a	18:12	18:33	18:23	12
2019/04/16	b	19:11	19:33	19:22	12
2019/04/16	c	20:14	20:35	20:25	11
2019/04/17	a	17:48	18:10	17:59	12
2019/04/17	b	18:52	19:14	19:03	12
2019/04/17	c	19:52	20:14	20:03	12
2019/04/17	d	20:51	21:06	20:59	8
2019/04/18	a	16:42	17:05	16:54	12
2019/04/18	b	17:43	18:05	17:54	12
2019/04/18	c	18:50	19:13	19:02	12
2019/04/18	d	19:57	20:20	20:09	12
2019/04/18	e	20:42	20:57	20:50	8
2019/04/19	a	17:11	17:34	17:23	12
2019/04/19	b	18:16	18:39	18:28	12
2019/04/19	c	19:17	19:39	19:28	12
2019/04/19	d	20:16	20:39	20:28	12
2019/04/20	a	17:16	17:38	17:27	12
2019/04/20	b	18:15	18:37	18:26	12
2019/04/20	c	19:15	19:37	19:26	12
2019/04/21	a	17:10.	17:29	17:20	8
2019/04/21	b	18:08	18:30	18:19	12
2019/04/21	c	19:12	19:35	19:24	12
2019/04/22	a	16:43	17:06	16:55	12
2019/04/22	b	17:45	18:08	17:57	12
2019/04/22	c	18:50	19:14	19:02	12
2019/04/22	d	19:51	20:14	20:03	12
2019/04/23	a	17:36	18:01	17:49	14
2019/04/23	b	18:38	19:01	18:50	12
2019/04/23	c	19:39	20:01	19:50	12
2019/04/24	a	17:23	17:46	17:35	12
2019/04/24	b	18:30	18:53	18:42	12
2019/04/24	c	19:33	19:56	19:45	12

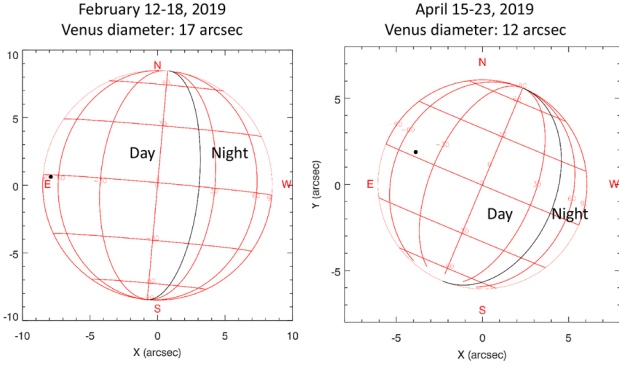**Notes.** The second column (a, b, c...) refers to the various maps recorded each day.

Fig. 1. Geometrical configurations of the disk of Venus during the two TEXES runs of February and April 2019. The terminator is indicated with a black line and the sub-solar point with a black dot. Both configurations show the morning terminator.
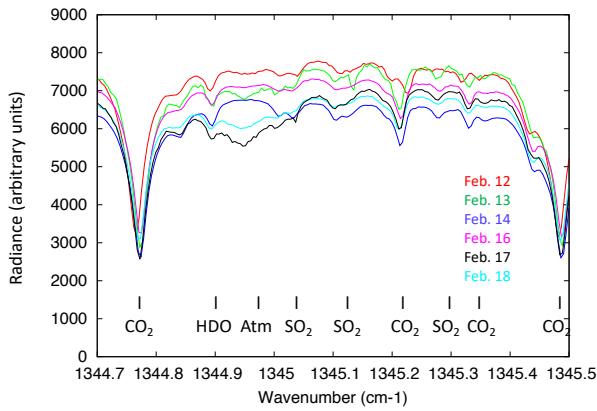

Fig. 2. Examples of disk-integrated spectra of Venus between 1344.8 and 1345.4 cm^{-1} (7.4 μm) recorded in February 2019. It can be seen that the broad terrestrial atmospheric absorption feature around 1344.95 cm^{-1} varies strongly from day to day.

Fig. 3. Examples of disk-integrated spectra of Venus between 1344.8 and 1345.4 cm^{-1} (7.4 μm) recorded in April 2019. Due to the strong terrestrial absorption around 1344.95 cm^{-1}, the depth of the HDO line at 1344.90 cm^{-1} could not be measured on April 21–24, 2019.

Fig. 4. Examples of maps of the line depth of the weak CO_2 transition at 1345.22 cm^{-1} (7.4 μm), corresponding to the observations shown in Figs. 2 and 3. The scale is the same for the two maps. The subsolar point is shown as a white dot. Times refer to the mid-times of the observations.

both correspond to the morning terminator. Figures 2 and 3 show representative disk-integrated spectra corresponding to the runs of February 2019 and April 2019, respectively. The spectral range (1344.8–1345.4 cm^{-1}) includes several weak SO_2 transitions, two weak CO_2 lines and one weak HDO line. As in our previous studies (see E19), we used the HDO line at 1344.90 cm^{-1}, the SO_2 multiplet at 1345.1 cm^{-1} and the CO_2 line at 1345.22 cm^{-1} in order to retrieve the H_2O and SO_2 mixing ratios directly from the line depth ratios. For the conversion from the line depth ratios (ldr) into the volume mixing ratios (vmr), the following equations were used (E16, E19):

– vmr (SO_2)(ppbv) = ldr (SO_2) × 600.0
– vmr (H_2O)(ppmv) = ldr (HDO) × 1.5.

To convert the HDO vmr into the H_2O vmr, we assume, above the clouds, a D/H ratio of 200 times the Vienna standard ocean water (VSMOW). We adopted this value in 2012, following Krasnopolsky (2010), as an averaged value from previous measurements (Bjoraker et al. 1992; Bertaux et al. 2007; Fedorova et al. 2008). We are aware of the uncertainty associated with this parameter (Krasnopolsky et al. 2013), but we keep the enrichment factor of 200 with respect to the terrestrial value for consistency within our analysis.

Figure 4 shows two maps of the CO_2 line depth, corresponding to each of our two observing runs. The CO_2 line depth gives us information o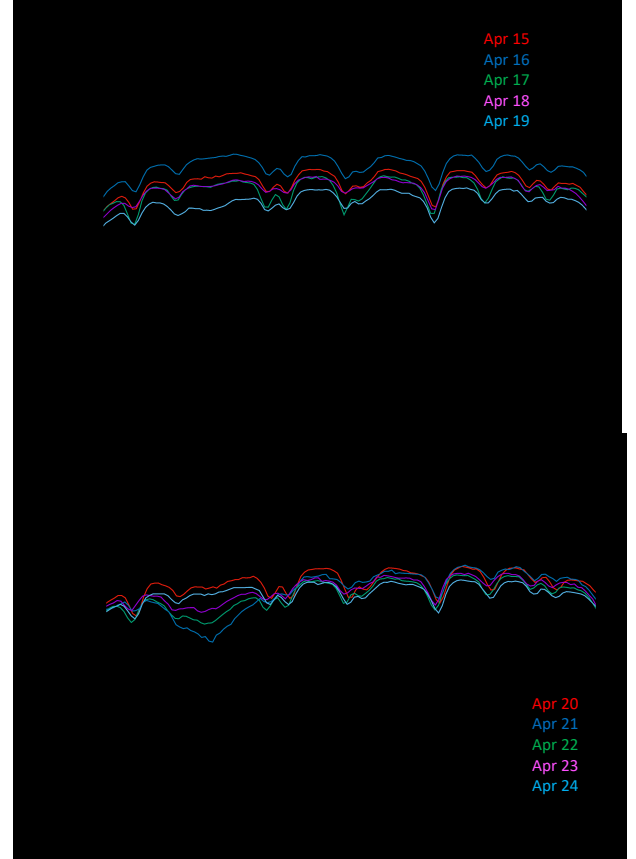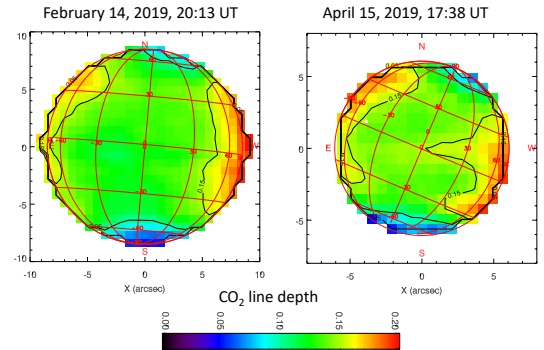n the temperature gradient just above the level which is probed in the continuum (E13, E16). As shown in Fig. 1, the 2019 data were recorded when the morning terminator was observed. As mentioned earlier, the signature of a thermal cooling at high latitude is expected at that time (see E13 and E16), so we would expect that the depth of the CO_2 lines would be zero or even negative at high latitudes, as observed in E13. Surprisingly, this effect does not clearly appear in Fig. 4. We already mentioned in E19 that the effect of the thermal cooling near the polar collars, clearly observed in E16 (2012–2016), does not appear systematically in the forthcoming observations. The analysis of
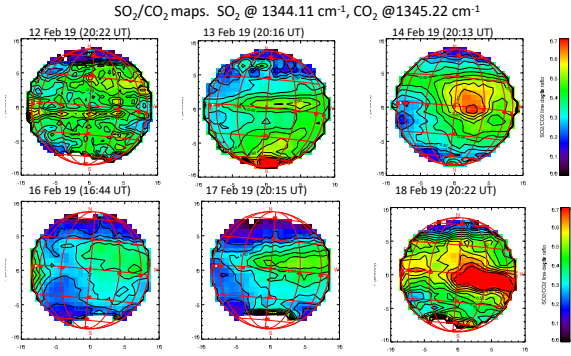
Fig. 5. Examples of maps of the line depth ratio of a weak SO_2 multiplet (around 1345.1 cm^{-1}) to the CO_2 transition at 1345.22 cm^{-1}, recorded in February 2019 (one map per observing day). Disk-integrated spectra corresponding to these maps are shown in Fig. 2. The sub-solar point is shown as a white dot. Times refer to the mid-times of the observations.
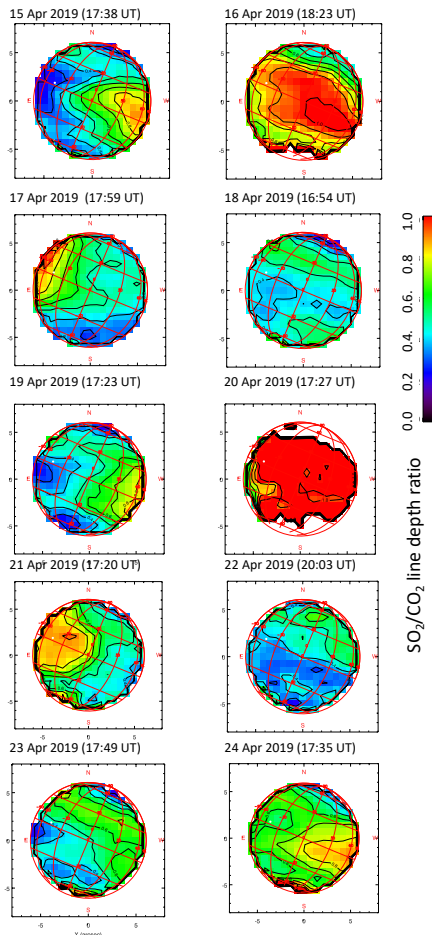

Fig. 7. Maps of the line depth ratio of a weak SO_2 multiplet (around 1345.1 cm^{-1}) to the CO_2 transition at 1345.22 cm^{-1}, recorded on April 16, 2019. The figure on the left (18:23 UT) is the same as in Fig. 6. The sub-solar point is shown as a white dot. Times refer to the mid-times of the observations.

Fig. 8. Maps of the line depth ratio of a weak SO_2 multiplet (around 1345.1 cm^{-1}) to the CO_2 transition at 1345.22 cm^{-1}, recorded on April 20, 2019. The figure on the left (27:27 UT) is the same as in Fig. 6, with a different scale. The sub-solar point is shown as a white dot. Times refer to the mid-times of the observations.

the transitions mentioned above. One map per day is shown, in February 2019 (Fig. 5) and in April 2019 (Fig. 6). As in previous cases, SO_2 variations are obvious, both locally over the Venus disk and on a time scale of 24 h.

As an illustration of the short-term behavior of the SO_2 plumes, Fig. 7 shows a time sequence of SO_2 at the cloud top on April 16, 2019. The figure shows the fast depletion of a strong SO_2 plume on a time scale of two hours. The peak intensity of the SO_2 plume is close to its maximum value over the whole 2012–2019 period.

A surprising example of the SO_2 distribution over the Venus disk is shown in Fig. 8. Two SO_2 maps, recorded on April 20, 2019 and separated by about one hour, show a very high SO_2 vmr all over the disk (near 600 ppbv, corresponding to a SO_2/CO_2 line depth ratio close to 1.0), with a local maximum, higher than 1 ppmv, near the sub-solar point, which decreases within a time scale of one hour. The location of the plume, near the sub-solar point, is unusual, as well as the local SO_2 maxima which might be due to some artifact. Near the limb, our retrieval method becomes very uncertain due to the large airmass factor. Previous analyses have shown that in the case of lines depths of 10 percent or less, the departure from linearity may induce an uncertainty of about 10 percent, and up to 20 percent at the limb (Encrenaz et al. 2015). In addition, the observations of April 2019 refer to the morning terminator. We have seen that, in this case, a temperature inversion is observed near the polar collars, making the retrieval of minor species very difficult at high latitude. This is

Fig. 6. Examples of maps of the line depth ratio of a weak SO_2 multiplet (around 1345.1 cm^{-1}) to the CO_2 transition at 1345.22 cm^{-1}, recorded in April 2019 (one map per observing day). Disk-integrated spectra corresponding to these maps are shown in Fig. 3. The sub-solar point is shown as a white dot. Times refer to the mid-times of the observations.

the thermal profile and its variations with time and longitude will be the topic of a forthcoming publication.

2.2. SO$_2$ maps

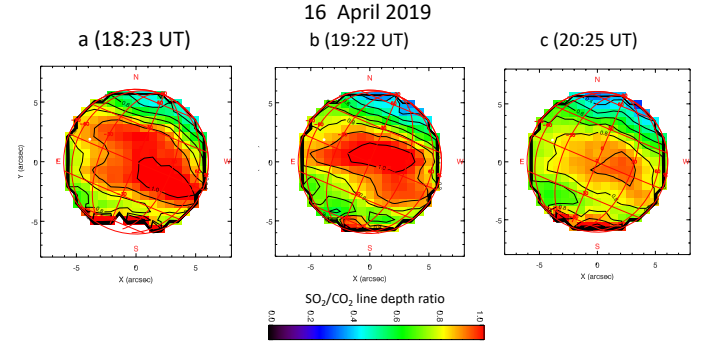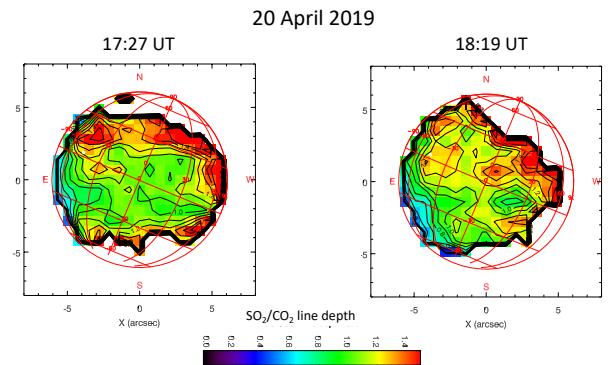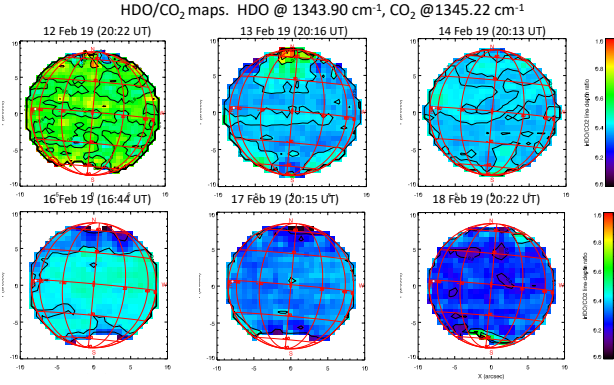Figures 5 and 6 show examples of maps of the SO_2 volume mixing ratio obtained from the data shown in Figs. 2 and 3, using

HDO/CO$_2$ maps. HDO @ 1343.90 cm^{-1}, CO$_2$ @1345.22 cm^{-1}

Fig. 9. Maps of the line depth ratio of the weak HDO transition (at 1344.90 cm^{-1}) to the CO$_2$ transition at 1345.22 cm^{-1}, recorded during the February 2019 run. Data are the same as in Figs. 2 and 5. The sub-solar point is shown as a white dot. Times refer to the mid-times of the observations.
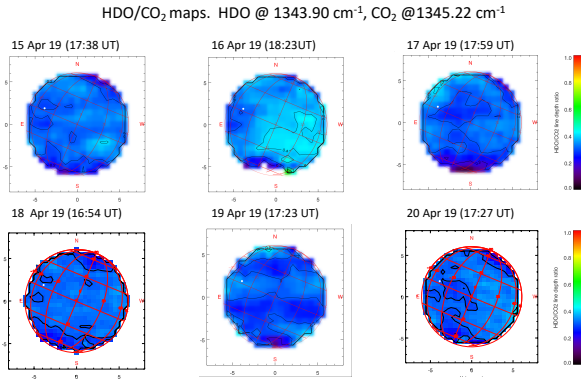
HDO/CO$_2$ maps. HDO @ 1343.90 cm^{-1}, CO$_2$ @1345.22 cm^{-1}

Fig. 10. Examples of maps of the line depth ratio of the weak HDO transition (at 1344.90 cm^{-1}) to the CO$_2$ transition at 1345.22 cm^{-1}, recorded during the April 2019 run. Data are the same as in Figs. 3 and 6. The sub-solar point is shown as a white dot. Times refer to the mid-times of the observations. Data of April 21–24 are not shown because the terrestrial atmospheric absorption (see Fig. 3) is too strong for the HDO retrieval to be reliable.

why the high latitude part of the map is not shown in the figure. In view of these uncertainties, the maps of April 18, 2019 have not been included in our statistical analysis (see below). Figure 8 illustrates the variety of behaviors shown by the SO$_2$ plumes, which are discussed in Sect. 5.

2.3. HDO maps

Figure 9 shows examples of HDO maps recorded in February 2019, corresponding to the same data as shown in Figs. 2 and 5. Figure 10 shows examples of HDO maps corresponding to the April 2019 run, using the data shown in Figs. 3 and 6. Only six HDO maps are shown in Fig. 10 because, due to the strong telluric absorption (Fig. 3), HDO could not be reliably measured in the data of April 21–24. As observed in our previous observations, the HDO maps are homogeneous over the disk, but the disk-averaged H$_2$O volume mixing ratio shows a global decrease with time, as compared with previous data (E13, E16, E19). As shown in Fig. 10, the disk-averaged H$_2$O mixing ratio, measured at the end of the February run and during the April run, is close to 0.5 ppmv (corresponding to a HDO/CO$_2$ line depth ratio around 0.3), i.e. lower than the maximum disk-averaged values of SO$_2$ observed on April 16 and 20, 2019. The time
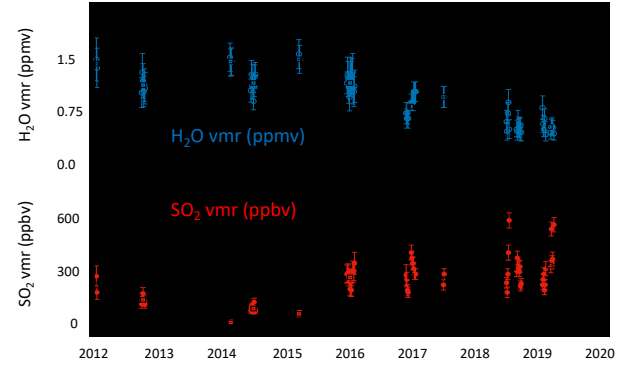

Fig. 11. Long-term variations of the H$_2$O volume mixing ratio (*top*, blue points), inferred from the HDO measurements, and the SO$_2$ volume mixing ratio (*bottom*, red points), measured at the cloud top from the TEXES data at 7.4 μm. A daily mean is shown in this figure. The black squares are the mean values of the H$_2$O and SO$_2$ mixing ratios averaged over each run. In 3 cases (Dec. 2017–Jan. 2018, July-Sept. 2018, Feb.–Apr. 2019), we have co-added all data (separated by less than 3 months), in order to have a more homogeneous time sampling over the long term.

variability of H$_2$O and its relationship with SO$_2$ are discussed in Sect. 5.

3. Long-term variations of the H$_2$O and SO$_2$ abundances at the cloud top

Figure 11 shows the long-term variations of H$_2$O and SO$_2$ since 2012. From 2012 to 2018, the data are the same as in E19, but we have chosen to show a single point per day because, as shown in E19, a SO$_2$ plume is most often observed over a full day. It can be seen that SO$_2$ exhibits larger and larger short-term variations as the mean disk-averaged abundance of SO$_2$ increases. In order to eliminate these short-term variations, we have also plotted the data using a single mean abundance of H$_2$O and SO$_2$ per run, and we have co-added the points separated by less than 3 months, which gives a total number of 10 points (Fig. 11). The data reveal, over the long term, an anti-correlation between H$_2$O and SO$_2$, with a correlation coefficient of -0.80. It is interesting to note that the anti-correlation is even stronger if the two first points, corresponding to 2012, are removed: indeed, if we consider only the 8 points between 2014 and 2019, the correlation coefficient is -0.90. The significance of this anti-correlation is discussed in Sect. 5.

4. A statistical study of the SO$_2$ plumes

Using the whole TEXES dataset between 2012 and 2019, we have performed a statistical study of the SO$_2$ plumes, with respect to their distribution as a function of latitude, longitude and local time. Then, we have extended this analysis to a study of the distribution of the SO$_2$ abundance with local time and longitude.

First, we consider the probability of SO$_2$ appearance as a function of local time (LT). The advantage of this method, already used in E19, is that it is independent of the mean disk-integrated SO$_2$ vmr; it thus allows us to disentangle LT variations from long-term temporal variations. Our method is the following. First, for each day of observation, we select one single map, the one showing the SO$_2$ plume with the strongest vmr. The choice of a single map per day allows us to remove short-term local variations, as it has been seen that a SO$_2$ plume has typically a life time of a few hours (thus being present over several

Table 2. Summary of TEXES observations obtained in 2019 and used for the analysis of the SO$_2$ plumes.

Date of obs.	Time (UT)	SEP E. long.	Max SO$_2$ E. long.	Min SO$_2$ E. long.	SSP E. long.	SEP LT (h)	Max SO$_2$ LT (h)	Min SO$_2$ LT (h)	Max SO$_2$ Latitude	Min SO$_2$ Latitude	SO$_{2max}$ (ppbv)
2019/02/12	21:38	200.7	280.2	235.2	130.2	7.3	5.0	2.0	25S	35S	350
2019/02/13	21:28	203.4	253.3	223.3	133.3	7.3	6.0	4.0	5N	5S	300
2019/02/14	20:13	205.9	233.7	218.7	136.2	7.4	6.5	5.5	5N	5S	420
2019/02/16	20:30	211.2	277.4	247.4	142.4	7.4	5.0	3.0	20N	5N	350
2019/02/17	22:38	214.2	265.7	250.7	145.7	7.4	5.0	4.0	10N	0	350
2019/02/18	21:54	217.2	253.9	223.9	148.9	7.4	7.0	5.0	5N	0	400
2019/04/15	17:38	6.1	125.1	95.1	320.1	8.9	3.0	1.0	15N	5S	540
2019/04/16	18:23	8.9	90.8	60.8	323.3	9.0	5.5	3.5	0	15S	660
2019/04/17	17:59	11.6	303.9	288.9	326.4	9.0	14.5	13.5	20N	0	540
2019/04/19	19:28	16.9	84.9	69.9	332.4	9.0	5.5	4.5	15N	15S	480
2019/04/21	17:20	22.2	16.0	346.0	338.5	9.1	11.5	9.5	20N	0	780
2019/04/22	20:03	24.9	86.5	56.5	341.5	9.1	7.0	5.0	20N	10N	360
2019/04/23	19.50	27.7	89.8	59.8	344.8	9.1	7.0	5.0	5N	5S	420
2019/04/24	17:35	30.6	100.4	85.4	347.9	9.2	5.5	4.5	10N	10S	480

Notes. Times refer to the mid-times of the observations. SEP and SSP refer to the sub-Earth point and the sub-solar point respectively. Max SO$_2$ E. long and Min SO$_2$ E. long define the longitude range where a SO$_2$ plume is observed. Max SO$_2$ LT and Min SO$_2$ LT define the local time interval where the SO$_2$ plume appears. SO$_{2max}$ indicates the SO$_2$ volume mixing ratio observed inside the interval where SO$_2$ is maximum.

maps of a given day), but does not last until the following day. On this map, we evaluate the LT range over which the SO$_2$ plume is present. We assign a probability of 1 within this range, and 0 outside this range. In parallel, we assign a probability of 1 over the whole observed LT range, i.e. a range of 12 h corresponding to the observed hemisphere of the planet. Then, for each LT, we do the summation of all maps for which this LT is observed (red curve in Figs. 13 and 18), and, separately, the summation of all maps for which a SO$_2$ plume is present at the given LT (blue curve in these two figures). Dividing the blue curve by the red curve gives us the probability for a SO$_2$ plume to be present at a given LT. The same method is applied below to calculate the probability of SO$_2$ appearance as a function of longitude (see below, Figs. 18 and 19).

Table 2 lists the new data from the February 2019 and April 2019 runs, which are a complement to the previous dataset shown in Table 2 of E19. This table gives, in sequence, for each observation, the longitude of the sub-Earth point (SEP), the longitude range of the observed SO$_2$ plume (corresponding to a probability of 1), the longitude of the sub-solar point (SSP), the LT of the SEP, the LT range and the latitude range of the SO$_2$ plume (where the probability is 1), and finally the SO$_2$ vmr within this plume. This last quantity is not used when we calculate the probability of SO$_2$ plume appearance, but is used in the next step. We note that two dates are missing, as compared with Table 1: April 18 (because no SO$_2$ maximum could be identified, as shown in Fig. 6), and April 20, because of the uncertainties mentioned above (Fig. 8).

4.1. Distribution of the SO$_2$ plumes as a function of latitude

Figure 12 (an update of Fig. 6 of E19) shows the distribution of the SO$_2$ plumes as a function of latitude. As observed previously, the distribution strongly peaks toward the equator, with most of the features appearing within the 30N–30S latitude range. This distribution is also observed in the SPICAV/Venus Express dataset, as shown in Fig. 9 of Marcq et al. (2020). In the case of TEXES, the identification of plumes at high latitude is more uncertain than around the equator, due to the peculiar shape of
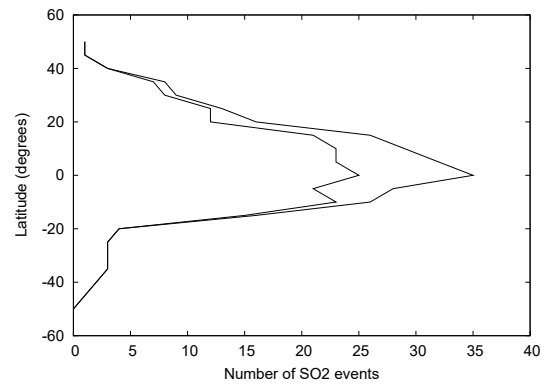

Fig. 12. Thick line: distribution of the location of the SO$_2$ plumes as a function of latitude. The total number of observations is 48. Observations at high latitudes (above 50N and 50S) are not considered, due to the uncertainty on the thermal profile in the regions of the polar collars. Thin line: distribution obtained without the 2019 data (Fig. 6 of E19).

the thermal profile around the polar collar when the morning terminator is observed; in this case, when the thermal profile becomes close to isothermal, the retrieval of SO$_2$ and HDO is no longer possible. For this reason, we limit our statistical analysis of the SO$_2$ plumes within 50 degrees of the equator.

4.2. Distribution of the SO$_2$ plumes as a function of local time

In this section, we estimate the probability of SO$_2$ plume appearance as a function of local time, using the method described above and the whole dataset of 48 points (2012–2019). Figure 13 shows the summation of all local times observed by TEXES over the 2012–2019 period, as well as the summation of all local times for which a SO$_2$ plume is present. It can be seen that the dayside is most observed, with a maximum around noon, while there are few observations around midnight. Figure 14 shows the probability of SO$_2$ plume appearance as a function of local time. A depletion appears around 10:00, with a clear enhancement around the terminators, confirming our earlier results. Between
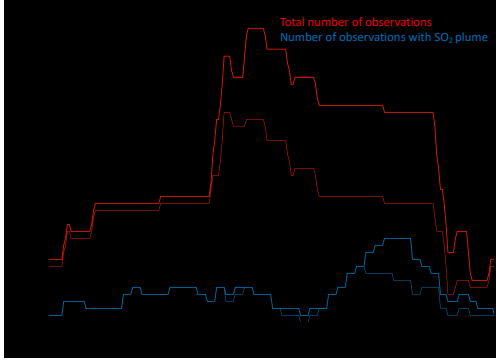
Fig. 13. Red curve: summation of all local times observed by TEXES over the 2012–2019 period, using the 46 observations listed in Table 1 of E19 and Table 2 of this paper. Blue curve: summation of all local times for which a SO$_2$ plume was present, using the same dataset. As in E19, the probability of SO$_2$ plume appearance is equal to 1 within the local time range of the maximum SO$_2$ and 0 elsewhere. Thick lines: Results with the whole dataset (2012–2019); thin lines: dataset without the 2019 data, as shown in Fig. 10 of E19.

Fig. 14. Probability of SO$_2$ appearance as a function of local time, calculated as the ratio of the blue curve to the red curve in Fig. 13. The error bar is proportional to $n^{-0.5}$, where n is the number of observations for which the local time is observed (red curve in Fig. 13). Thick points: Results with the whole dataset (2012–2019); thin points: dataset without the 2019 data, as shown in Fig. 10 of E19.

22:00 and 03:00, we consider that the statistics are too low for the result to be significant.

It must be reminded that the analysis described above considers only the location of the SO$_2$ plumes as a function of local time, and not their intensity. As mentioned above, its main advantage is that it separates the study of the probability of SO$_2$ appearance as a function of LT from the study of the long-term temporal variations: indeed all observations have the same weight, whatever the disk-integrated SO$_2$ vmr is. However, this analysis does not allow us to compare our results with those of other instruments using occultation techniques like SPICAV/Venus Express, which do not have the capability of mapping the planet instantaneously.

In a second step, we try to estimate the distribution of the SO$_2$ vmr as a function of LT, although we are aware that long-term variations of SO$_2$ might have some incidence on our result. In order to incorporate this second parameter in our analysis, instead of using the probability of SO$_2$ plume occurence, we now consider the SO$_2$ vmr as a function of local time, estimated as follows. We have two observable parameters: (1) within the LT interval of the SO$_2$ plume, we measure the SO$_2$ vmr (SO$_{2\text{max}}$), equal to its maximum value (as given in Table 1 of E19 and Table 2 of this paper); (2) we measure the integrated
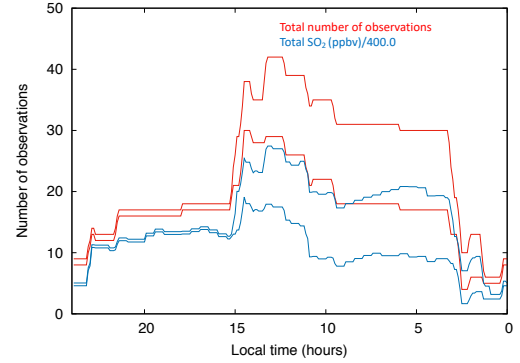

Fig. 15. Thick red curve: summation of all LT observed by TEXES over the 2012–2019 period. This curve is the same as the red curve in Fig. 13. Thick blue curve: summation of all SO$_2$ vmr distributions vs LT, using the same dataset. For each observation, the distribution of the SO$_2$ vmr as a function of local time is calculated as described in the text. The sum of all SO$_2$ vmrs has been divided by 400.0 ppbv; this number corresponds to a typical value of the SO$_2$ vmr within the plumes over the whole period (see last column of Table 2); this normalization allows us to show both curves on the same scale. Thin lines: results using the dataset without the 2019 runs (34 points).

value of the SO$_2$ vmr over the observable LT interval (SO$_{2\text{moy}}$), as being equal to the disk-average SO$_2$ vmr, inferred from the disk-integrated spectra (Figs. 2, 3 and 11). If s is the LT fraction of the SO$_2$ plume appearance (with s between 0 and 1), the mean SO$_2$ vmr outside the plume (SO$_{2\text{min}}$) is such that

$$SO_{2\text{max}} \times s + SO_{2\text{min}} \times (1 - s) = SO_{2\text{moy}}$$
or
$$SO_{2\text{min}} = [SO_{2\text{moy}} - s \times SO_{2\text{max}}] / (1 - s)$$

Figures 15 and 16 show the results, using both the whole dataset (2012–2019) and the 2012–2018 dataset (i.e. with the 34 points used in E19). Since the maximum SO$_2$ vmr is usually not more than twice its disk-integrated value, the distribution curve of the SO$_2$ vmr as a function of local time is considerably smoother than the probability curve shown in Fig. 14. A depletion is still observed on the morning side (10:00) and the two local maxima near the terminators are still present. In addition, an increase of the SO$_2$ abundance is observed from the morning to the evening. In order to check the validity of this result, we also made this calculation using the median of the SO$_2$ volume mixing ratio instead of its average. Using the median is a way to give less weight to possible outliers associated with isolated plumes. Calculations show that the shape of both curves is identical. These results are discussed in Sect. 5.

In order to better analyze the possible relation between the SO$_2$ vmr and the local time, we used a second approach based on the long-term variations of SO$_2$ at the cloud top. Figure 17 shows a plot of the disk-averaged SO$_2$ vmr (same data as in Fig. 11), as a function of the diameter of the Venus disk. A diameter of 10 arcsec corresponds to the dayside fully illuminated, whereas a diameter of 60 arcsec (never observed because of the solar elongation constraint of the telescope) would correspond to the full night side. It can be seen that there is no apparent correlation nor anti-correlation between the Venus diameter and the disk-integrated SO$_2$ vmr; the correlation coefficient between these two quantities (calculated over the 13 runs) is 0.0. The conclusion is that there is no evidence for a difference between the dayside and nightside distributions of SO$_2$.

We also wondered whether the disk-integrated SO$_2$ vmr might be correlated with the type of the observed terminator
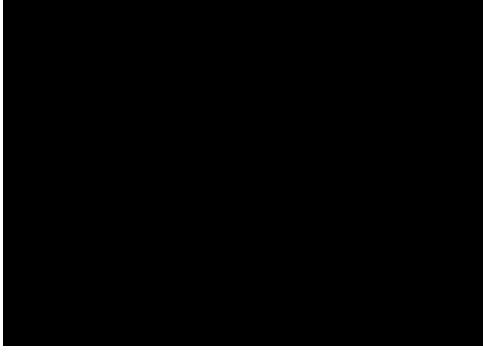
Fig. 16. Thick points: distributions of the SO_2 vmr as a function of local time, calculated as the ratio of the blue curve to the red curve in Fig. 15. The error bar is proportional to $n^{-0.5}$, where n is the number of observations for which the local time is observed (red curve in Fig. 15). Thin points: results using the dataset without the 2019 runs (34 points).
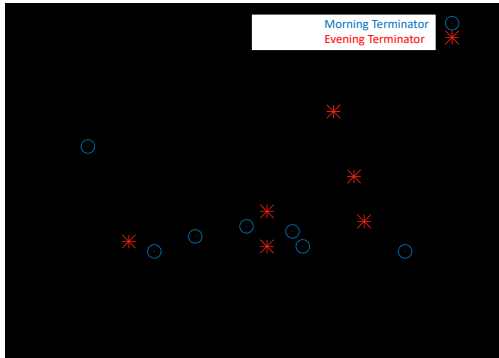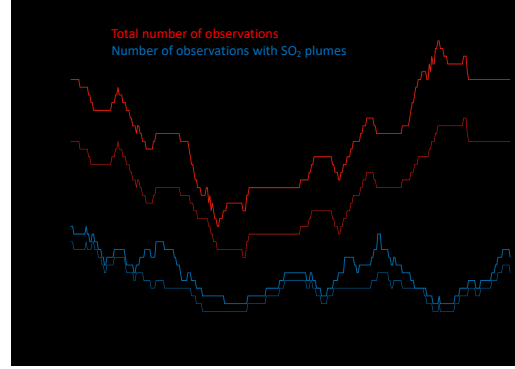

Fig. 18. Red curve: summation of all longitudes observed by TEXES over the 2012–2019 period, using the 48 observations listed in Table 2. Blue curve: summation of all longitudes where a SO_2 plume was present, using the same dataset.
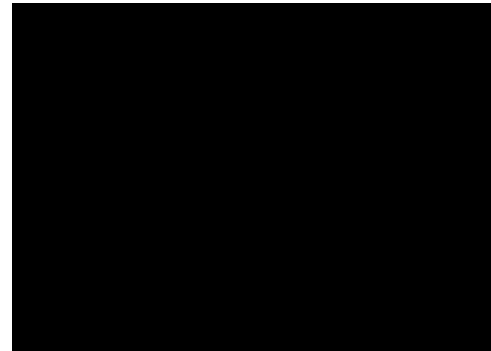

Fig. 17. Disk-integrated SO_2 vmr (x-axis, same data as in Fig. 11) plotted as a function of the diameter of the Venus disk (y-axis). Blue circles: morning terminator; red crosses: evening terminator.

Fig. 19. Probability of SO_2 appearance as a function of longitude, using the data shown in Table 1 of E19 and Table 2 of this paper. The error bar is proportional to $n^{-0.5}$, where n is the number of observations for which the longitude is observed (red curve in Fig. 18). Thick points: Results with the whole dataset (2012–2019); thin points: dataset without the 2019 data.
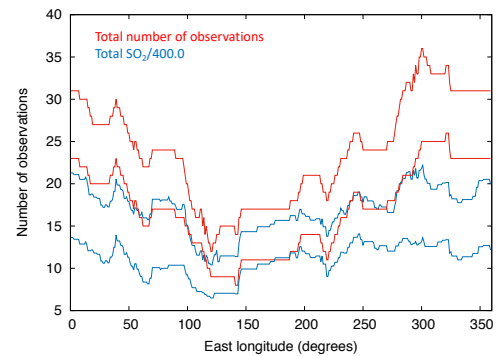
(morning or evening, see Fig. 17). Again, the absence of correlation is apparent. To calculate the correlation coefficient, we assigned a coefficient equal to 0 for the morning terminator and 1 for the evening terminator. In this case, the correlation coefficient is very weakly positive (0.24). Although it may be too weak to be significant, we note that this result is consistent with the slight increase observed for the SO_2 vmr around the evening terminator, as shown in Fig. 16.

4.3. Distribution of the SO_2 plumes as a function of longitude

We have completed our analysis of the SO_2 distribution as a function of longitude, using the same method as described in E19 and using the 48 data points available (Table 1 of E19 and Table 2 of this paper). Results are shown in Figs. 18 and 19. We have added all observable longitude ranges to obtain the longitude visibility curve corresponding to our dataset. In the same way, we have added all longitude ranges where a SO_2 plume was present (Fig. 18). Dividing this curve by the longitude visibility curve gives us the probability of SO_2 appearance as a function of the longitude (Fig. 19). As in our previous study, there is no clear trend in the longitudinal distribution of the probability of SO_2 plume appearance, except a possible depletion around 300 E.

As a next step, we have determined the SO_2 vmr distribution as a function of longitude, using the same method as described in the previous section. Results are shown in Figs. 20 and 21. It can be seen that the SO_2 vmr distribution shows a regular curve

Fig. 20. Red curve: summation of all longitudes observed by TEXES over the 2012–2019 period. This curve is the same as the red curve in Fig. 18. Blue curve: summation of all SO_2 vmr distributions vs longitude, using the same dataset. For each observation, the normalized distribution of the SO_2 vmr as a function of longitude is calculated as described in the text. The sum of all SO_2 vmrs has been divided by 400.0 ppbv. Thick points: results with the whole dataset (2012–2019); thin points: dataset without the 2019 data.

with a maximum around 120–200 E and a minimum around 300–350 E. It can be noticed that the region of SO_2 maximum is near the region of Aphrodite Terra where the highest equatorial volcanoes are located. The significance of this result is discussed below (Sect. 5).

Fig. 21. Distribution of the SO$_2$ vmr as a function of longitude calculated as the ratio of the blue curve to the red curve in Fig. 20. The error bar is proportional to $n^{-0.5}$, where n is the number of observations for which the longitude is observed (red curve in Fig. 20). Thick points: Results with the whole dataset (2012–2019); thin points: dataset without the 2019 data.

5. Discussion

5.1. Comparative evolution of SO$_2$ and H$_2$O

When the TEXES campaign started in 2012, the disk-integrated SO$_2$ vmr at the cloud top was 200–300 ppbv, i.e. about a fifth of the H$_2$O vmr (Fig. 11). In 2014 and 2015, the disk-integrated SO$_2$ abundance decreased down to 100 ppbv or less, while the water abundance remained more or less constant. Since 2015 until now, we observe a regular decrease of H$_2$O and a long-term increase of the SO$_2$ abundance, up to a disk-integrated vmr above 300 ppbv, with local plumes as high as 800 ppbv (Table 2 and Figs. 5–8). In parallel, the short-term variations of SO$_2$ observed in 2018 and 2019 tend to be stronger than in the previous years. This suggest that the long-term evolution of the SO$_2$ abundance at the cloud top is associated with the short-term activity of the SO$_2$ plumes, as also observed by SPICAV aboard Venus Express (Marcq et al. 2020). It is interesting to note that the H$_2$O vmr at the cloud top remained more or less constant between 2012 and 2015, and then started to decrease. This is consistent with the observations of Venus Express in the near-infrared range (Cottini et al. 2015, Fedorova et al. 2016) which found no evidence for temporal variations at the cloud top during the lifetime of the Venus Express mission (2006–2015).

Using the 2018 and 2019 data, for which SO$_2$ and H$_2$O exhibit comparable abundances, we can wonder why SO$_2$ exhibits strong short-term variations, both locally and as a function of time, whereas these variations are not observed in the HDO maps. Indeed, Figs. 9 and 10 confirm our previous statement about the local homogeneity of the HDO maps: the disk-integrated vmr of water vapor decreases with time, but remains remarkably constant over the Venus disk. If the SO$_2$ plumes are associated with convective motions, we need to understand why the same behavior is not observed in the HDO maps. Possibly, the explanation is linked to the much larger vertical gradient of SO$_2$ than that of H$_2$O within the clouds, since SO$_2$ varies by a factor of 1000 and H$_2$O by only a factor of 30 between the bottom and the top of the Venus clouds (Bézard & De Bergh 2012). This difference implies that the signature of vertical transport should be more visible in the SO$_2$ field than for H$_2$O. SO$_2$ is also a sink for H$_2$O through the formation of H$_2$SO$_4$, so an increase in H$_2$O is not expected when a plume of SO$_2$ is observed.

For the first time, our data show evidence for a long-term anti-correlation between the SO$_2$ and H$_2$O abundances at the cloud top. The anti-correlation is maximum if we consider only the 2014–2019 time interval, which suggests that some long-term process is at work within the Venus atmosphere below and/or above the clouds. It is interesting to note that this anti-correlation does not appear on short-term scales of hours or days. This is illustrated by a comparison between Figs. 5 and 9 which show daily variations of the SO$_2$ and H$_2$O abundances during the February 2019 run: the H$_2$O abundance decreases regularly from Feb. 12 to 18, 2019 whereas the SO$_2$ maps show two local maxima on Feb. 14 and 18. In addition, for these two dates, the H$_2$O maps remain uniform over the Venus disk, while SO$_2$ maps show a high contrast driven by the emergence of SO$_2$ plumes. In summary, the long-term anti-correlation observed between the SO$_2$ and H$_2$O abundances seems to be disconnected from the short-term activity of the SO$_2$ plumes.

Photochemical models have been developed to model the behavior of water vapor and sulfur dioxide at the cloud top and within the clouds of Venus (Parkinson et al. 2015). Using a 1D chemistry-diffusion model (Zhang et al. 2012), Shao et al. (2020) have found that the anti-correlation of SO$_2$ and H$_2$O at 64 km can be generally explained by the sulfur chemistry in the middle atmosphere (58–100 km) of Venus. Even when SO$_2$ and H$_2$O vary randomly at the middle cloud top (58 km), their model finds that the two species at 64 km are mostly anti-correlated, because SO$_2$ and H$_2$O modulate each other through the sulfuric acid formation and intermediate SO$_3$ reactions at 64 km. In contrast, a change of the eddy diffusivity in the middle atmosphere cannot explain the SO$_2$–H$_2$O anti-correlation. While the anti-correlation itself can be explained by the sulfur chemistry, the cause for the variations of species abundances at the middle cloud top is not understood. These variations may relate to atmospheric processes inside or below the clouds, as tracer transport (Marcq et al. 2013, Bierson & Zhang 2020) or geological processes on the surface, as volcanic eruption (Esposito 1984). The TEXES-observed long-term variations of SO$_2$ and H$_2$O may thus contain additional information for mechanisms of how the two species co-vary deeper in the Venus atmosphere. Additional observations and modeling work will allow the processes inside and below the clouds to be unraveled.

5.2. Variations of SO$_2$ as a function of local time

Using the 2019 data described in this paper, we have completed our analysis of the probability of SO$_2$ plume occurence as a function of local time. Results shown in Fig. 14 confirm our previous conclusion (E19) about the two maxima around the terminators. We have performed an analysis of the SO$_2$ abundance as a function of local time. Not surprisingly, the variations are significantly smoothed, simply because the maximum SO$_2$ vmr within a plume is never more than twice its disk-integrated value. In contrast, the change in the shape of the curve (Fig. 16) is more surprising. The SO$_2$ vmr at the evening terminator is higher than at the morning terminator by a factor of about 30 percent.

It can be seen from Fig. 16 that the agreement with the results of SPICAV (Fig. 10 of Marcq et al. 2020) is not as good as observed previously. Indeed, in E19, we pointed out the good agreement between these data and the TEXES results (Fig. 19 of E19). However, the TEXES curve was the probability of SO$_2$ plume occurence, while the SPICAV data referred to the SO$_2$ vmr as a function of local time. Thus, we would have expected a better agreement between the SPICAV curve and our new calculation of the SO$_2$ vmr as a function of local time (Fig. 16 of this paper). This is actually not the case: the SPICAV data show a contrast by a factor 10 between the SO$_2$ vmr around noon and its

value at the terminators, while this contrast is less than a factor 2 in the TEXES data (Fig. 16). However, taking into account the error bars of both data sets, the two results are still consistent. The origin of the difference might be the altitude shift in the levels probed by the two experiments, as the UV data of SPICAV probe a few kilometers above the cloud top, and also the different epochs explored by the SPICAV and TEXES data sets. Also, it can be noticed that, since the SPICAV observations refer to a single point on the Venus disk (while the TEXES data show a global map), it is more difficult, in the case of SPICAV, to disentangle the temporal variations from the local ones. Further comparison with the UV data of Akatsuki will be useful to investigate this issue.

As shown in Figs. 13 and 15, the TEXES dataset still lacks a good coverage of the nightside. We have analyzed the variations of the disk-integrated SO_2 as a function of the diameter of Venus, in order to search for a possible correlation between the SO_2 abundance and the illuminated fraction of the disk (Fig. 17). With a correlation factor of 0.0, this comparison shows that there is no evidence for a change of the SO_2 abundance with respect to day or night.

5.3. Variations of SO_2 as a function of longitude

Figure 19 shows the probability of SO_2 plume appearance as a function of longitude. It is very similar to our previous analysis (Fig. 9 of E19A) and shows no clear dependence with longitude, except a possible minimum around 300° east longitude. In contrast, the variations of the SO_2 vmr as a function of longitude (Fig. 21) shows a smooth curve with a distinct maximum around 120–200° east longitude, i.e. near the region of Aphrodite Terra. This figure is to be compared with the SPICAV results (Fig. 11 of Marcq et al. 2020). In this case, there is no agreement between the two datasets as, in the case of SPICAV, the SO_2 vmr is maximum around 30–60° east longitude. In both cases, it is difficult to disentangle the spatial and temporal variations of SO_2. In addition, in the case of the TEXES data, we note that the SO_2 vmr distribution (Fig. 21) and the probability of SO_2 occurrence (Fig. 19), as a function of longitude, show very different shapes, which is not the case for the SO_2 variations as a function of local time. In summary, our result regarding the SO_2 distribution as a function of longitude should be considered with caution and has yet to be confirmed.

5.4. Comparison of the SO_2 statistical analysis with our previous results

In this section, we analyze how our statistical analysis of the SO_2 plumes is affected by the inclusion of the 2019 dataset, which adds 14 new points to our previous list of 34 observations. In the case of the analysis of the SO_2 plumes as a function of local time (LT), the addition of the 2019 dataset significantly improves the statistics in the morning side of the planet (LT = 03:00–12:00; Fig. 13). The probability of SO_2 plume appearance as a function of LT is only slightly modified and the error bars are lowered (Fig. 14). Because of the limited number of observations between 23:00 and 03:00, we do not consider the probability of SO_2 plume appearance to be significant in this time interval. In contrast with Fig. 14, the variations of the SO_2 volume mixing ratio as a function of LT show a significant difference when the 2019 dataset is added (Fig. 16). The effect is probably due to the increase of the disk-integrated SO_2 vmr between 2015 and 2019 (Fig. 11). This illustrates the difficulty of disentangling the long-term global variations of SO_2 from its distribution
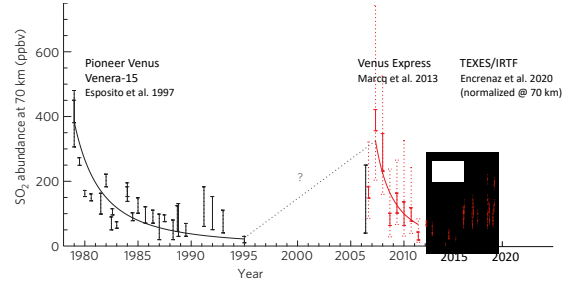

Fig. 22. Long-term variations of the SO_2 volume mixing ratio at the cloud top of Venus between 1989 and 2020, as reported by Esposito et al. 1997, Marcq et al. (2013, 2020) and this paper (Fig. 11). The figure is adapted from Marcq et al. (2013).

as a function of local time. It confirms that, for this analysis, the probability of SO_2 plume appearance is a more reliable indicator.

In the case of the statistical study of the SO_2 plumes as a function of longitude, the addition of the 2019 dataset is uniformly distributed over all longitudes (Fig. 18). The probability of SO_2 plume appearance (Fig. 19) has the same shape as in E19, with the error bars being reduced. The distribution of the SO_2 vmr shows a maximum around 120–200° east longitude but, as pointed out above, this result remains to be confirmed. Figure 21 shows that this maximum is significantly reduced when the 2019 dataset is added, and, as mentioned above, the distribution of the SO_2 vmr as a function of longitude cannot be easily separated from long-term temporal variations.

5.5. Long-term variations of SO_2 between 1979 and 2019

Thanks to the monitoring of the SO_2 vmr achieved in the UV by Pioneer Venus (Esposito et al. 1997) and Venus Express (Marcq et al. 2013), and in the IR by Venera-15 (Zasova et al. 1993) and later TEXES, we now have information on the long-term variations of the SO_2 abundance at the cloud top of Venus over a 40-year period. Figure 22 shows the SO_2 long-term variations measured by the spacecraft between 1979 and 2014 (Marcq et al. 2013, 2020), completed with the disk-averaged SO_2 abundance measured by TEXES between 2012 and 2020. As in E19 and in Marcq et al. (2020), we rescale the TEXES measurements by dividing the TEXES data by a factor 3, to account for the altitude difference between the UV observations (about 70 km) and the IR observations (about 64 km). It can be seen that, after the two maxima observed by Pioneer Venus in 1980 and by Venus Express in 2008, followed by a continuous decrease during 5–7 yr, the mean SO_2 abundance at the cloud top has been continuously increasing since 2015, but is still about half the maximum value reached in 1980 and 2008. In addition to this long-term trend, as mentioned above, we note that, as observed by both SPICAV and TEXES, the short-term variations observed in the SO_2 plumes tend to increase as the disk-integrated abundance of SO_2 increases. Future monitoring with Akatsuki and TEXES will hopefully allow us to continue this analysis in the future.

6. Conclusions

In this paper, we have pursued our SO_2 and HDO monitoring at the cloud top of Venus using the TEXES instrument at 7.4 μm by adding new data obtained in February and April 2019, and we have reanalyzed the whole TEXES dataset between 2012 and

2019 to study (1) the long-term behavior of H$_2$O and SO$_2$, and (2) the behavior of SO$_2$ as a function of latitude, local time and longitudinal. The main results of this study can be summarized as follows.

– An anti-correlation is visible in the long-term variations of H$_2$O and SO$_2$ at the cloud top, with a correlation coefficient of -0.80 (-0.90 between 2014 and 2019). On short timescales, this anti-correlation is hidden behind the short-term variations due to the SO$_2$ plumes which appear and disappear within a few hours.

– Since 2015, we observe a long-term decrease of H$_2$O, associated with a long-term increase of SO$_2$. At the same time, the short-term variations of SO$_2$ due to the SO$_2$ plumes become larger and larger, as shown in Fig. 11. For the first time, we observe in July 2018, a SO$_2$ plume showing a local vmr of 800 ppbv, corresponding to a disk-integrated SO$_2$ vmr of 600 ppbv, equal to the H$_2$O vmr derived at the same time. However, we do not see evidence for an anti-correlation between SO$_2$ and H$_2$O on short-term (hours or days) time scales.

– The new analysis of the probability of SO$_2$ plume occurence as a function of local time confirms our previous results (E19) with two maxima around the terminators. The distribution of the SO$_2$ vmr as a function of local time shows the same trend, with a local minimum occurring in the morning (10:00 local time). However, the maximum around the evening terminator is more pronounced than the one around the morning terminator.

– As in our previous analysis, the probability of SO$_2$ plume occurence as a function of longitude shows no clear feature, except a possible minimum around 300 E. In contrast, the distribution of the SO$_2$ vmr as a function of longitude shows a clear maximum between 120 E and 200 E, in the volcanic region of Aphrodite Terra. However, this result is not confirmed by the SPICAV analysis (Marcq et al. 2020), and should be considered with caution. More generally, we need to insist on the complexity of the SO$_2$ behavior, which exhibits both short-term and long-term variations, and we emphasize the difficulty of disentangling the local time variations of SO$_2$ from its longitude variations.

In the future, we plan to develop the comparison with past SPICAV and on-going Akatsuki UV data to test the validity of our conclusions regarding the variations of the SO$_2$ abundance, and in particular its dependence as a function of longitude. A comparative analysis of the two TEXES datasets, at 7.4 μm and 19 μm, as initiated in E13 and E16, should also allow us to better constrain the SO$_2$ behavior within the H$_2$SO$_4$ cloud.

References

Belyaev, D. A., Montmessin, F., Bertaux, J.-L., et al. 2012, Icarus, 217, 740

Bertaux, J.-L., Vandaele, A.-C., Korablev, O., et al. 2007, Icarus, 217, 740

Bézard, B. & De Bergh, C., 2012, J. Geophys. Res., 112, E04S07

Bierson, C. J., & Zhang, X., 2020, J. Geophys. Res. Planets, submitted

Bjoraker, G. L., Larson, H. P., Mumma, M. J., et al. 1992, BAAS, 24, 995

Cottini, V., Ignatiev, N. I., Piccioni, G., et al. 2015, Planet. Space Sci., 113, 219

Encrenaz, T., Bézard, B., Greathouse, T. K., et al. 2004, Icarus, 170, 424

Encrenaz, T., Greathouse, T. K., Roe, H., et al. 2012, A&A, 543, A153

Encrenaz, T., Greathouse, T. K., Richter, M. J., et al. 2013, A&A, 559, A65

Encrenaz, T., Greathouse, T. K., Lefèvre, F., et al. 2015, A&A, 578, A127

Encrenaz, Greathouse, T. K., Richter, M. J., et al. 2016, A&A, 595, A74

Encrenaz, Greathouse, T. K., Marcq, E., et al. 2019, A&A, 595, A70

Esposito, L. W. 1984, Science, 223, 1072

Esposito, L. W., Bertaux, J.-L., Krasnoposly, V., et al. 1997, in Venus II: Geology, Geophysics, Atmosphere, and Solar Wind Environment, Chemistry of lower atmosphere and clouds, eds. Bougher, S. W., Hunten, D. M., & Phillips, R. J. (Tucson, AZ : University of Arizona Press), 415

Fedorova, A., Korablev, O., Vandaele, A.-C., et al. 2008, J. Geophys. Res., 113, E00B25

Fedorova, A., Marcq, E., Luginin, M., et al. 2016, Icarus, 275, 143

Krasnopolsky, V. A. 1986, Photochemistry of the atmospheres of Mars and Venus (New York: Springer-Verlag)

Krasnopolsky, V. A. 2007 Icarus, 191, 25

Krasnopolsky, V. A. 2010, Icarus, 209, 314

Krasnopolsky, V. A., Belyaev, D. A., Gordon, I. A., et al. 2013, Icarus, 224, 57

Lacy, J. H., Richter, M. J., Greathouse, T. K., et al. 2002, PSAP, 114, 153

Marcq, E., Bertaux, J.-L., Montmessin, F., et al. 2013, Nat. Geosci. 6, 25

Marcq, E., Mills, F. P., Parkinson, C. P., & Vandaele, A. C., 2018, Space Sci. Rev. 214, 10

Marcq, E., Jessup, K. L., Baggio, L., et al. 2020, Icarus, 335, 11368

Mills, F. P., Esposito, L. W., & Yung, Y. K. 2007, Geophys. Mongraph Ser., 176, 73

Parkinson, C., Gao, P., Esposito, L., et al. 2015, Planet. Space Sci., 112, 226

Shao, W. D., Zhang, X., Bierson, C. J., et al. 2020, J. Geophys. Res. Planets, submitted [arXiv:2006.09522]

Rohlfs, K., & Wilson, T. L. 2004 Tools for radioastronomy, 4th edn. (Berlin: Springer)

Vandaele, A.-C., Korablev, O., Belyaev, D., et al. 2017a, Icarus, 295, 16

Vandaele, A.-C., Korablev, O., Belyaev, D., et al. 2017b, Icarus, 295, 1

Zhang, K., Liang, M. C., & Mills, F. P. 2012, Icarus, 217, 714

Zasova, L. V., Moroz, V. I., Esposito, L. W., & Na, C. Y. 1993, Icarus, 105, 92